Surface & Coatings Technology 367 (2019) 1–10

Contents lists available at ScienceDirect

Surface & Coatings Technology

journal homepage: www.elsevier.com/locate/surfcoat

Multiscale experimental characterization of coatings on ceramics: A case study of tungsten on SiC☆

Huaxin Li[a], Takaaki Koyanagi[b,*], Xunxiang Hu[b], Yutai Katoh[b]

[a] Hefei University of Technology, Hefei 230009, China
[b] Oak Ridge National Laboratory, Oak Ridge, TN 37831, USA

ARTICLE INFO

Keywords:
Coating
Multiscale characterization
Micro-mechanical testing
Transmission Kikuchi diffraction

ABSTRACT

State-of-the-art transmission Kikuchi diffraction (TKD) and high-speed nano-indentation were combined with glow-discharge optical emission spectroscopy (GDOES), transmission electron microscopy (TEM) and micro-cantilever testing to characterize microstructures and mechanical properties of coatings on a ceramic substrate. The goal was to develop a multiscale experimental characterization method to assess the coating/substrate couple. A tungsten coated silicon carbide substrate was the system used for this development. The combination of GDOES, TEM and TKD enabled precise phase identification in the system, while TKD provided superior spatial resolution for phase identification. Micro-cantilever tests were able to measure adhesion strength, with support from high-speed nano-indentation which enabled rapid modulus and hardness determination over relatively large areas.

1. Introduction

Ceramics have emerged as useful materials in many engineering applications, taking advantage of high melting points, high hardness and strength, durability, and chemical inertness among other attractive attributes [1]. To achieving superior performance in service environments, a surface coating on the substrate ceramic is frequently adopted to improve the resistance of wear, corrosion, impact, or irradiation [2]. For example, a tungsten (W) coating on a silicon carbide (SiC) composite is capable of protecting the SiC/SiC composite from high surface temperature and erosion due to sputtering when it is used as a divertor structure in a fusion reactor system [3].

Coating technologies have had extensive development, and the adhesion mechanisms can be categorized as interfacial adhesion, inter-diffusion adhesion, intermediate layer adhesion and mechanical interlocking adhesion [4]. Among these mechanisms, diffusion adhesion usually exhibits relatively high adhesion strength. It is widely accepted that the coating adhesion is strongly affected by the interfacial microstructure, including interfacial bonding defects and interfacial property mismatch (e.g. coefficient of thermal expansion (CTE) and elastic modulus). Reliable evaluation methods are essential to understand the microstructure and coating adhesion of coating/ceramic substrate systems.

Microstructural characterization including phase identification is a vital part of understanding coating/ceramic substrate systems, since the difference in phase structure results in the interfacial properties mismatch. This is especially important for diffusion bonded coatings because the dual character of the inter-diffusion layer contributes to interface bonding and enhances property mismatch via the formation of interfacial reaction phases. Precise phase identification usually integrates elemental analysis and determination of crystal structure. Tkadletz et al. summarized the latest advanced characterization methods for phase identification for hard coating systems [5]. Glow-discharge optical emission spectroscopy (GDOES), Auger electron and X-ray photoelectron spectroscopy (AES and XPS), secondary ion mass spectrometry (SIMS), Rutherford backscattering spectroscopy (RBS), elastic recoil detection analysis (ERDA), energy- or wavelength-dispersive X-ray spectroscopy (E/WDS), and atom probe tomography (APT) have all been applied to elemental analysis of coating systems. GDOES, AES, XPS, SIMS, RBS and ERDA offer the possibility of accurate

☆ This manuscript has been co-authored by UT-Battelle, LLC under Contract No. DE-AC05-00OR22725 with the U.S. Department of Energy. The United States Government retains and the publisher, by accepting the article for publication, acknowledges that the United States Government retains a non-exclusive, paid-up, irrevocable, world-wide license to publish or reproduce the published form of this manuscript, or allow others to do so, for United States Government purposes. The Department of Energy will provide public access to these results of federally sponsored research in accordance with the DOE Public Access Plan (http://energy.gov/downloads/doe-public-access-plan).

* Corresponding author.
E-mail address: koyanagit@ornl.gov (T. Koyanagi).

https://doi.org/10.1016/j.surfcoat.2019.03.040
Received 19 December 2018; Received in revised form 3 March 2019; Accepted 18 March 2019
Available online 20 March 2019
0257-8972/

depth-resolved measurements for most elements including light elements [6–8]. AES, XPS, RBS and ERDA are applicable to elemental depth profiling of the coating with thickness less than a few microns. GDOES enables rapid elemental depth profiling at macro-scale area for thick coatings even for the thickness over 100 μm, but can only provide relatively low lateral resolution (~1 mm). SIMS is capable of giving a better lateral resolution (~100 nm) for elemental depth profiling of the coatings with thickness range of nanoscale to microscale, but can only offer relatively low sputtering speed (~10 μm/h) [8]. E/WDS is a common technology for elemental analysis at the microscale, EDS has a shorter acquisition time in elemental analysis than WDS, but the energy resolution of EDS (~130 eV) is worse than that of WDS (~10 eV). APT enables accurate elemental analysis at the atomic scale, but the analyzed area is limited to the nanoscale [9]. Since these available options for elemental distribution analysis apply at various scales, the selection of elemental analysis methods depends on the specific requirement in a practical application. X-ray diffraction (XRD), transmission electron microscopy (TEM) and electron back-scattered diffraction (EBSD) are methods frequently adopted for crystal structure analysis. XRD is only capable of providing information averaged over numerous grains without in-situ microstructural observation capability. TEM gives excellent spatial resolution (< 1 nm), but can only offer highly localized information. EBSD is a powerful tool for crystal orientation mapping, phase imaging, determination of grain size distributions and strain analysis, but is restricted by the sampled source volume to spatial resolution on the order of 25–100 nm and is not adequate to characterize nanocrystalline structures [10]. Cross-sectional X-ray nanodiffraction (CSnanoXRD) has also been applied to crystal structure analysis of coating and offers a relatively better lateral resolution of ~30 nm [11], but CSnanoXRD requires access to a synchrotron source, which greatly limits its widespread application. These techniques for crystal structure analysis leave a spatial resolution gap between EBSD and TEM. In this study, we introduce state-of-the-art transmission Kikuchi diffraction (TKD) for crystal structure analysis of coating system, which will fill the spatial resolution gap between EBSD and TEM by providing better spatial resolution (2–5 nm) while still retaining the advantages of EBSD in crystal structure analysis.

Coating adhesion is one of the most important concerns for a coating/substrate system. Numerical and experimental analyses are two available approaches for assessing coating adhesion. Numerical analysis is capable of simulating the stress, strain, deformation, and so on inside the coating/substrate system under external loads, providing insight into the fracture behavior of a coating/substrate system. Understanding fracture mechanisms is useful in optimizing coating designs. For instance, Li et al. developed a semi-analytical model to predict the stress evolution within a multilayer coating system during cyclic thermal loading by means of numerical analysis [12]. In addition, the interfacial fracture behavior of a double-ceramic-layer thermal barrier coating system with a segmented structure can be clarified via numerical analyses, as reported by Li et al. [13]. In experimental analyses, interfacial fracture toughness and adhesion strength are frequently measured for evaluation of coating adhesion [4]. Because interfacial fracture toughness gives a lower bound of crack initiation and propagation, and adhesion strength offers an upper bound of fracture failure. Indentation tests [14], four-point bend tests [15] and Brazilian disk tests [16] allow measurement of the interfacial fracture toughness of coating, with the interfacial fracture toughness usually depending on the failure mode [4]. Scratch tests attempt to establish an accurate relationship between the measured critical load and the actual adhesion strength, but it only provides a semi-quantitative determination of adhesion strength [17]. Peel tests are also unable to accurately measure the adhesion strength, because the applied force not only separates the coating from the substrate, but also plastically deforms the coating and overcomes friction [6,18]. These conventional evaluation methods are useful, but incapable of providing precise adhesion strength. With the development of the technology, integrating nano-indentation and focused ion beam (FIB) techniques attract extensive attention due to its superior performance in nano- and micro-mechanical properties evaluation. This combination is now widely used for measuring the basic mechanical properties of materials at small scales, including elastic modulus [19], yield stress [20], and fracture properties [21]. For example, the FIB-milling of micro-cantilever beams enables testing for the accurate determination of strength, fracture toughness analysis, and in-situ observations, which overcome the drawback of conventional evaluation methods on small-scale sample. This attractive evaluation method has been successfully used on single crystal materials [20], ion-irradiated materials [22], coating materials [23], etc. So far the micro-cantilever testing has not been commonly used to evaluate coatings on ceramics, particularly for diffusion bonded coating/ceramics substrate systems. In this study, we propose a method to advance micro-cantilever testing by using it in combination with state-of-the-art high-speed nano-indentation testing. We found this to be very useful for evaluating adhesion of a thin coating layer on a ceramic substrate, although the testing area/volume is limited due to the scale of the technique.

Our goal in this work was to demonstrate a multiscale experimental characterization scheme to assess the coating on ceramic substrate through capturing the microstructure and adhesion strength by using state-of-the-art TKD and high-speed nano-indentation, together with conventional methods previously applied for coatings, including GDOES, TEM and micro-cantilever testing. The feasibility of this multiscale experimental scheme was verified by application to a typical coating-on-ceramic system, namely W coating on a SiC substrate (hereinafter referred to as W/SiC).

2. Experimental

2.1. Fabrication of W coating on SiC substrate

Chemical vapor deposited (CVD) SiC (high resistivity grade, 99.9995% purity, Dow Chemical Company) was machined to disc shape samples with diameter 19.40 mm and thickness 1 mm. The surface of a SiC sample was polished up to 1 μm diamond suspension. An as-rolled W foil (25 μm, 99.95% purity, Goodfellow) was polished to a surface finishing on P800 SiC paper to clean the oxide from the surface. Both materials were then ultrasonically cleaned in an acetone bath for 10 min and dried in air.

A graphite paper/W/SiC/graphite paper “sandwich” was assembled in a standard graphite die (outer diameter: 50 mm and inner diameter: 20 mm) for spark plasma sintering (SPS, Model 25–10, Thermal Technology LLC) joining. The SPS joining was conducted with a heating rate of 100 °C/min in vacuum (< 0.1 Pa) with constant direct current used for heating. The temperature during the SPS process was measured by infrared pyrometer focused on a near-through-hole in the graphite die. A pressure of 30 MPa was applied on the sample during heating. The sample was held at 1300 °C for 10 min, then a cooling rate of 50 °C/min was set and the pressure decreased to 15 MPa as the temperature fell to room temperature. At room temperature, the pressure was removed and then the sample was taken from the SPS furnace. The resulting sample of W/SiC had a diameter of 19.40 mm and a thickness of ~1.025 mm, as shown in Fig. 1.

2.2. Mechanical property evaluations

The NanoBlitz 3D nano-indentation mapping of W/SiC was performed in a TESCAN MIRA3 scanning electron microscope (SEM) using a Nanomechanics InForce 1000 Actuator with a diamond Berkovich tip. A 16 × 40 array of indentations with an applied target load of 5 mN was centered on the W/SiC interface with an area of 40 μm × 100 μm. The indentation spacing was set as 2.5 μm. The indent speed of the nano-indentation mapping was about 1 s per indent.

Micro-cantilevers of the W/SiC interfacial zone were fabricated using a FEI Quanta 3D 200i Dual Beam FIB with a beam energy of

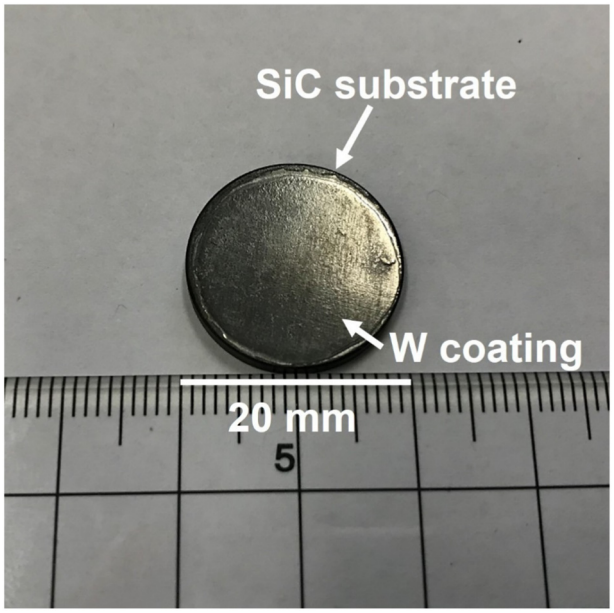

Fig. 1. Appearance of W/SiC after SPS process.

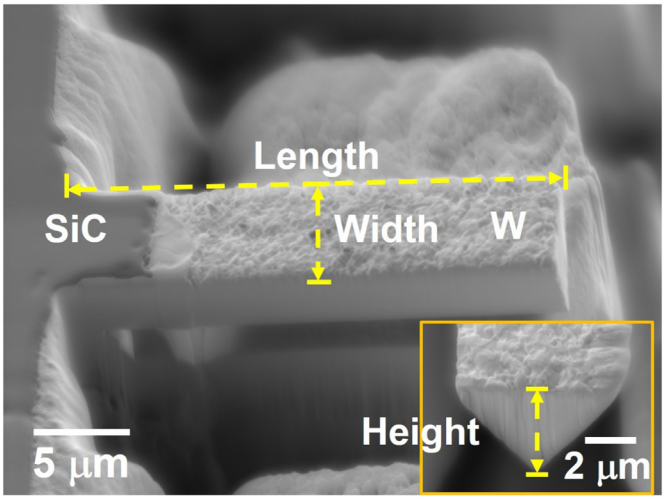

Fig. 2. SEM images of a typical micro-cantilever beam after FIB milling.

30 kV. In the first step, the specimen was tilted to 52° and a beam current of 30 nA was used to mill a "U" shape trench of width 15 μm, length 27 μm, and depth 10 μm, with a central arm 27 μm long and 10 μm wide. Next, a low beam current of 5 nA was used to mill the width of the central arm to approximately 5.5 μm. Then, the specimen was tilted to 22° and a diminishing beam current from 7 nA to 3 nA was used to undercut the central arm. After that, the specimen was rotated 180° to undercut the central arm from the opposite side using the same beam currents. As a final stage, to ensure all the cantilevers had a good surface, a lower beam current of 1 nA was used to clean the cantilevers. The dimensions of the final cantilevers were a central arm with 27–25 μm length, 4.3–6.6 μm width, and a triangle cross-section 2.1–3.4 μm in height. The meanings of the length, width and height in micro-cantilever beam are shown in Fig. 2. Details of the processing to fabricate these micro-cantilevers can be found elsewhere [21].

The micro-cantilever bend test was carried out on a Nanomechanics InForce 1000 Actuator with a diamond flat punch (diameter 10 μm) in the TESCAN SEM. The micro-cantilevers were loaded at a constant displacement rate of 10 nm/s. The length of loading point covering the micro-cantilever was approximately 5 μm. Five successful micro-cantilever beams were fabricated for bend testing.

2.3. Microstructural characterizations

Elemental depth profiling of W/SiC was accomplished using a Horiba GD profiler equipped with a laser differential interferometry profiling (DiP) system. A 4 mm-anode was used for the measurement. The argon gas pressure was 850 Pa and the power was 50 W for all measurements. Prior to the measurement, the space between the anode and the sample was flushed with high pressure Ar gas to purge any air. The wavelengths of the emission lines used by GDOES to determine the elements of interest are as follows: W (429.46 nm), Si (288.16 nm), and C (156.14 nm). Measurements were made every 0.1 s and the data collection lasted for at least 500 s, leading to a crater depth of 40 μm. The anode diameter of 4 mm defined the size of the sputtered region. After GDOES testing, the crater depth was inspected with a Keyence VHX-1000 digital microscopy.

The cross-sectional microstructure of the W/SiC was examined using a TESCAN MIRA3 SEM. TEM lamella were prepared using the FEI Quanta FIB operated at 30 kV for rough milling and 2 and 5 kV for final thinning, followed by low-energy ion milling in a Fischione Model 1040 NanoMill operated at 600 and 900 eV. The TEM observations were conducted using a JEOL JEM2100F in TEM mode and a FEI Talos F200X in scanning TEM (STEM) mode. Both TEMs were operated at 200 kV. The energy peaks used for EDS analysis are: C (K_α = 0.277 keV), Si (K_α = 1.739 keV) and W (L_α = 8.396 keV). The selected-area electron diffraction patterns were processed using Crystal Maker software. TKD analysis of the TEM specimens used an Oxford Instruments Nordlys detector on a FEI Versa 3D SEM/FIB operated with a beam current of 45 nA at 30 kV. TKD data was acquired using an Oxford Nordlys EBSD camera and Oxford Aztec 3.1 software. Post-processing analysis used Aztec, Oxford Tango software.

3. Results

3.1. Microstructural characterization

Fig. 3 shows the 3-D image of a crater observed by digital microscopy after GDOES testing and the associated elemental depth profiles of W/SiC measured by GDOES. The elemental distribution profile was measured on the macro-scale area of specimen surface (approximately 12.6 mm^2), defined by the 4 mm anode (Fig. 3a). The carter depth (to the blue bottom plane) determined by the digital microscope was approximately 40 μm, which was consistent with the Dip measurement (Fig. 3a). The initial sharp peaks in the GDOES depth profile were due to fluctuations of the Ar plasma (Fig. 3b). Owing to elemental inter-diffusion at the interface, two reaction layers were observed on both sides of W. The formation of the reaction layer on the left side was due to diffusion of C from the graphite paper, while the formation of the right side reaction layer was ascribed to the inter-diffusion of W, Si and C, forming the bond between W and SiC. The average reaction layer thickness on left and right sides was about 2 μm and 5 μm, respectively (Fig. 3b). It should be pointed out that the reaction layer formed between the W and the protective graphite paper (left side in this case) could be removed by polishing if the W-SiC was to be used in a system application. It is noted that the slopes of the three element concentration profiles in the inter-diffusion zone were not constant due to the changes of the sputtering rate as the chemical composition data evolves.

Fig. 4 shows the cross-sectional microstructure of W/SiC. This typically general overview of the W/SiC joint (Fig. 4a) shows the W/SiC was well-bonded and free from micro-scale discontinuities. In high magnification images, typified by Fig. 4b, the reaction layer, distinguished by the contrast of back scattered electrons (BSE) imaging, was approximately 3 μm thick. It is also apparent that C diffused further into the bulk W, rationalizing the observation that GDOES showed a

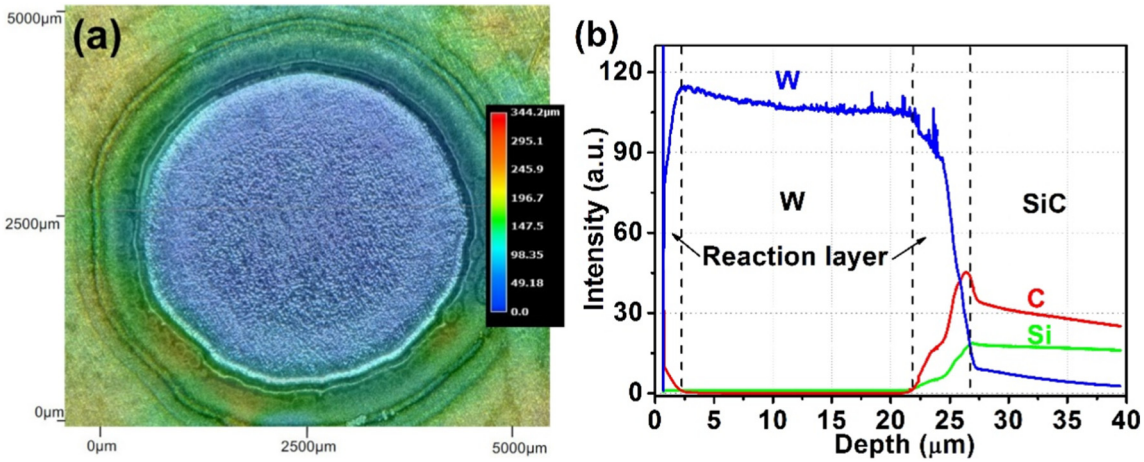

Fig. 3. (a) The 3-D image looking into the crater produced by the GDOES analysis, observed by quick Keyence optical microscopy after GDOES testing. The blue area is the crater bottom plane. (b) Elemental depth profiles of W/SiC measured by GDOES. (For interpretation of the references to color in this figure legend, the reader is referred to the web version of this article.)

larger reaction layer (5 μm thick) compared to the reaction layer (3 μm thick) observed by BSE imaging. The possible reasons is that GDOES testing showed an average diffusion depth at the macro-scale, while BSE analysis showed a local thickness of reaction layer at the micro-scale. The thickness difference between the reaction layer measured by GDOES and observed by BSE was only approximately 2 μm, which could be still regarded as consistent with differences between macro-scale and micro-scale analysis. No micro-cracks were observed in the coating, probably due to the similar CTE of SiC (CTE: $4.0 \times 10^{-6} K^{-1}$ [24]) and W (CTE: $4.5 \times 10^{-6} K^{-1}$ [25]), and the relatively thin thickness of the reaction layer.

The reaction layer consisted of two phases (gray-black and gray-white in Fig. 4) recognized from color contrast. Based on the principles of SEM imaging by BSE (Fig. 4b), the gray-black phase should contain the element with low atomic number, while the gray-white phase was assumed to contain the element with high atomic number. According to the elemental diffusion profile of W/SiC interface (Fig. 3), the Si and C elements diffused into W to form the reaction layer. Combining the GDOES and SEM results suggests that the gray-black and gray-white phases are carbide and silicide phases, respectively. This was also confirmed by the analysis presented below.

To clearly identify the phases constituting the reaction layer, the FIB-milled W/SiC specimen was analyzed using TEM and TKD. Fig. 5 shows the TEM analysis results. The STEM-HADDF (Fig. 5a) and STEM-EDS (Fig. 5b) images suggest that there were carbide and silicide, two different phases, in the reaction layer. After the precise element distributions were obtained, the same FIB-milling specimen was evaluated using TKD for crystal structure analysis, as shown in Fig. 6. The reaction layer consisted of two phases recognized from the band contrast image in Fig. 6a. The grain sizes of the reaction phase were in the range of 200 nm to 1.8 μm. The Euler map (Fig. 6b) shows no grain texture, which affects the interpretation of the nano-indentation modulus shown in Section 3.2. The phase map in Fig. 6c indicates the carbide phase in the reaction layer was W_2C. Its corresponding TKD pattern is seen in Fig. 6e, which is consistent with TEM-EDS analysis. The silicide phase in the reaction layer could not be identified by TKD analysis because of the poor quality of the TKD pattern without clear Kikuchi lines (Fig. 6d). To obtain more detailed information for the silicide phase, the same specimen was analyzed using TEM diffraction, as shown in Fig. 5(c and d). Two selected-area electron diffraction patterns were obtained from different directions of grain A (a grain of the silicide phase), and they are in good agreement with the W_5Si_3 phase patterns simulated by Crystal Maker software. Therefore, the silicide phase was determined to be a W_5Si_3 phase. This result was consistent with the other grains investigated. TEM diffraction analysis suggested no strong grain texture in the W_5Si_3. The detailed crystal structure information for the identified phases is summarized in Table 1. Consequently, the reaction phases are believed to consist of W_2C and W_5Si_3 after multiscale microstructural characterization.

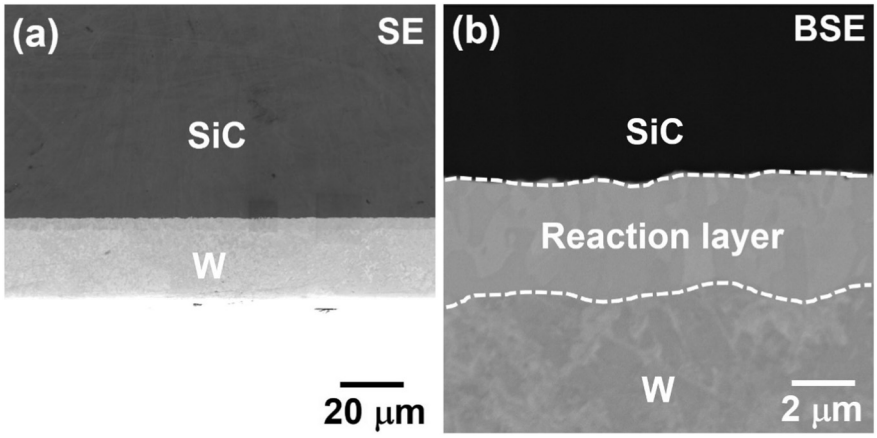

Fig. 4. Cross-sectional microstructure of W/SiC, (a) low magnification SEM-SE image, (b) high magnification SEM-BSE image.

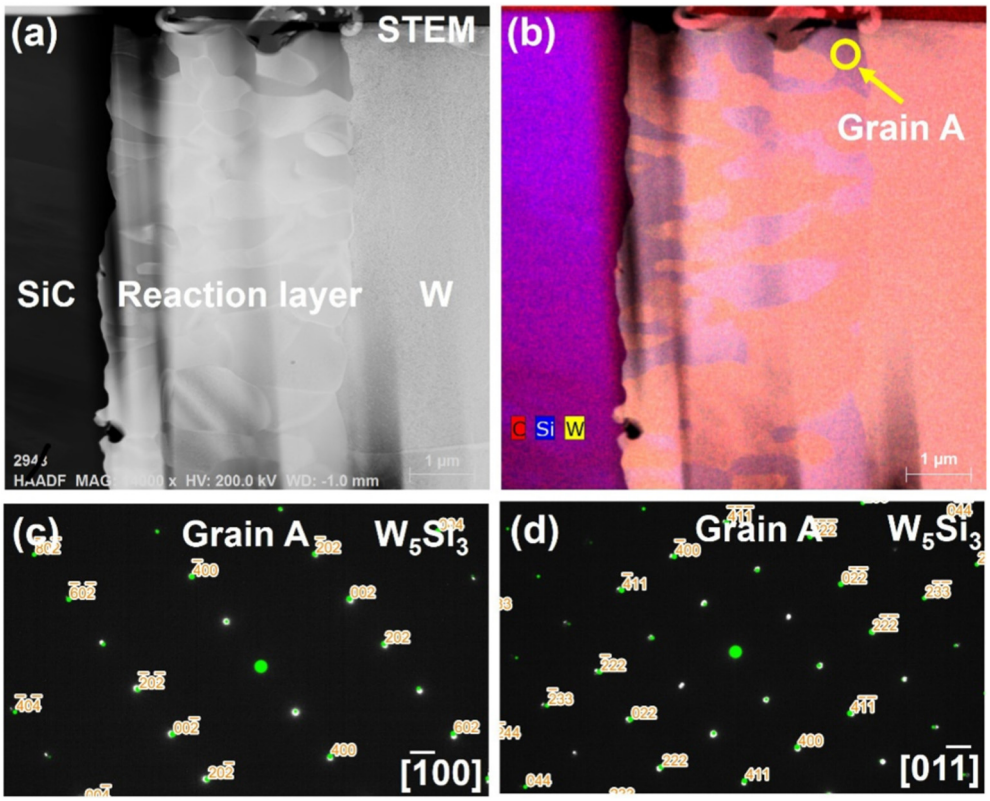

Fig. 5. TEM analysis of W/SiC, (a) STEM-HAADF image, (b) corresponding EDS maps, (c)–(d) electron diffraction patterns taken at grain A from different direction. The energy peaks used for EDS analysis are: C (K_α = 0.277 keV), Si (K_α = 1.739 keV) and W (L_α = 8.396 keV).

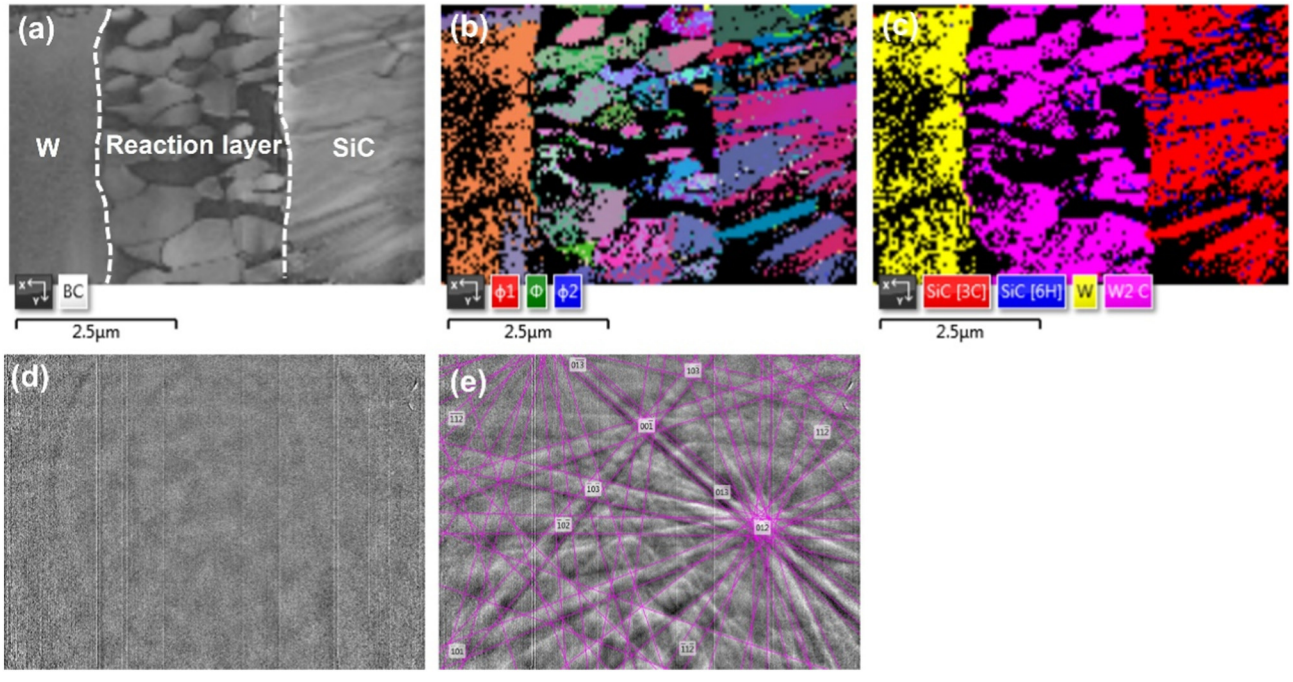

Fig. 6. TKD analysis of W/SiC, (a) band contrast image, (b) phase map, (c) Euler color map, (d) TKD pattern of black phase in reaction layer in band contrast image, and (e) TKD pattern of gray phase in reaction layer in band contrast image.

3.2. Micro-mechanical properties

Fig. 7 shows the SEM images of W/SiC after NanoBlitz 3D mechanical property mapping and the corresponding nano-hardness and modulus maps. Because of the high indent speed (~1 s per indent) of nano-indentation mapping, a 16 × 40 array of indentations could be completed around 10 min, which was a significant improvement over previous instruments, and enabled rapid data acquisition from a large test area. It can be clearly seen that all of the nano-indentations had an appropriate distance (indentation spacing > 3 × contact diameter) to

Table 1
Summary of detailed crystal structure information for phases identified by TKD and TEM diffraction analysis.

	Crystal structure	Space group	a, b, c (Å)	α, β, γ (°)
SiC-3C	Cubic (FCC)	216	a = b = c = 4.36	α = β = γ = 90
α-W	Cubic (BCC)	229	a = b = c = 3.08	α = β = γ = 90
W_2C	Orthorhombic	60	a = 4.73 b = 6.01 c = 5.19	α = β = γ = 90
W_5Si_3	Tetragonal	140	a = 9.611 b = 9.611 c = 4.967	α = β = γ = 90

Table 2
Summary of average hardness and modulus of each phase and reaction layer at room temperature in this work and in the literatures.

	Hardness (GPa)	Hardness (GPa) [Ref.]	Modulus (GPa)	Modulus (GPa) [Ref.]
CVD-SiC	34.24 ± 4.28	32.5–40.6 [24]	325.99 ± 25.22	461–466 [26]
W	10.02 ± 1.96	6.6–8.8 [27]	299.05 ± 43.74	320–410 [28]
Reaction layer	12.53 ± 6.16	/	281.14 ± 32.64	/

adjacent nano-indentations and were exactly loaded on the W/SiC interface (Fig. 7(a and b)), showing that the nano-mechanical properties of W/SiC could be accurately obtained by NanoBlitz 3D mechanical property mapping. The nano-hardness and elastic modulus maps (Fig. 7(c and d)) indicate the significant difference of the nano-hardness values at the W/SiC interface, while the elastic modulus across the W/reaction layer interface appeared to exhibit only small differences. There were some extremely low values in the hardness and modulus mapping, which indicate these indentations located at surface defects. To obtain more precise nano-hardness and elastic modulus values for each phase, statistical analysis was carried out on the data after excluding outliers. The data obtained in this work and in the literatures are summarized in Table 2. We used averaged nano-indentation modulus and hardness values to compare because no grain texture was found, based on the TKD Euler map (Fig. 6b). It has been reported that crystallographic orientation affects the nano-indentation modulus and hardness [29]. The nano-hardness and elastic modulus were in a good agreement with that in the literatures evaluated by nano-indentation technique. The lower elastic modulus of SiC in this work compared with the product sheet of SiC could be ascribed to the indentation size effect caused by the strain gradient plasticity in the sample. W and the reaction layer exhibited similar modulus values, even though a complex multi-phase structure exists in the W/reaction layer interface. Therefore it was reasonable to treat the W/reaction layer as a homogeneous material for calculation of bending strength.

A schematic drawing of the micro-cantilever bending test is shown in Fig. 8, and an actual micro-cantilever is imaged before and after

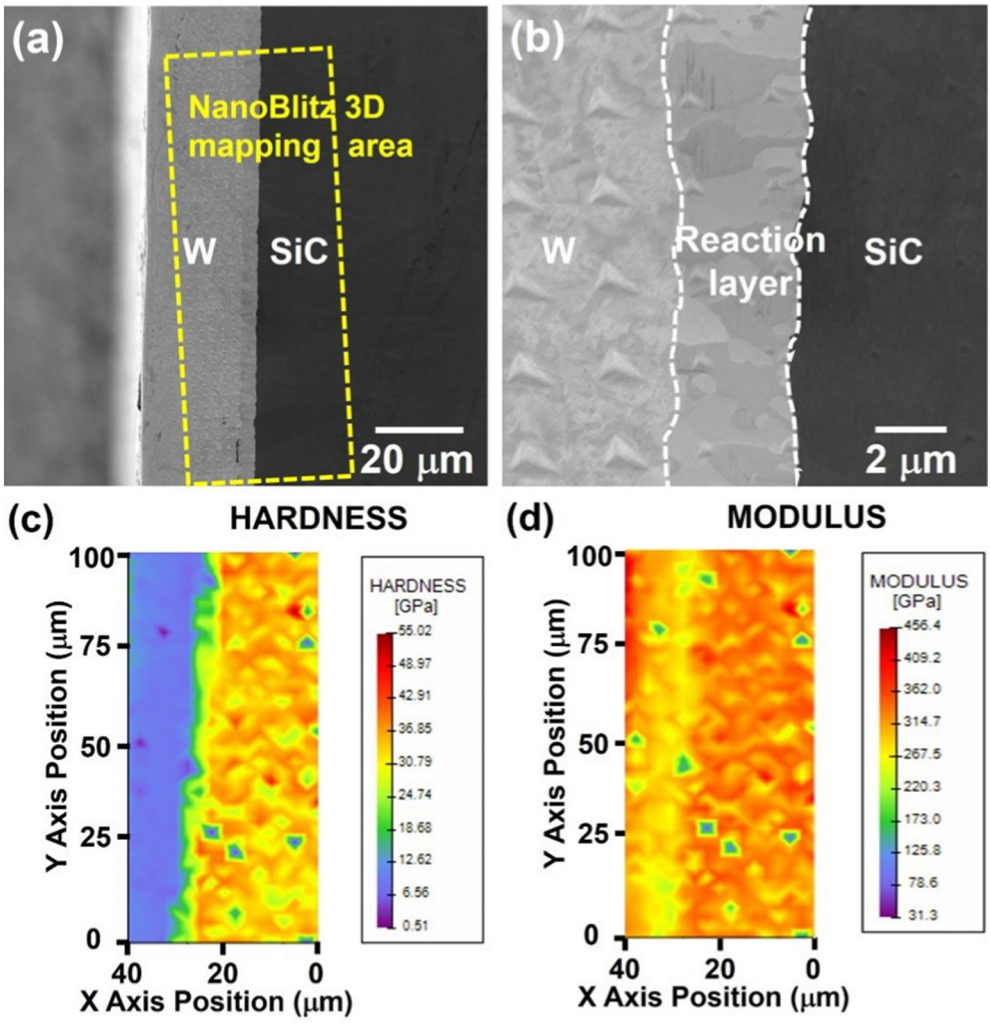

Fig. 7. NanoBlitz 3D mechanical property map of W/SiC interface, (a) low magnification SEM image after testing, (b) high magnification SEM image after testing, (c) hardness map, (d) modulus map. The regular pattern of the 680 indentations are clearly visible in (a) and (b).

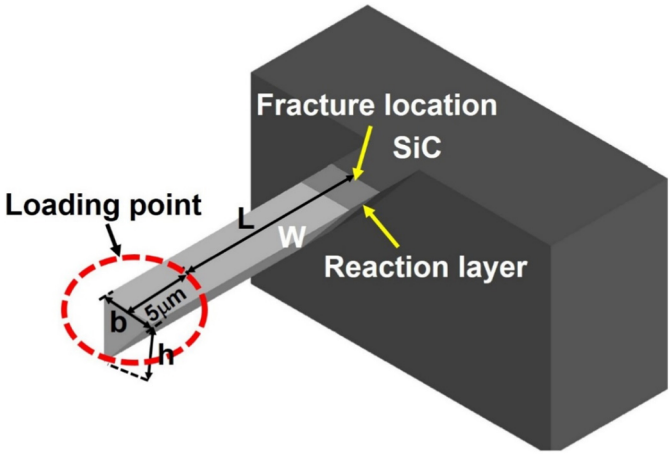

Fig. 8. The schematic plot of micro-cantilever bending testing.

bending testing from two directions is shown in Fig. 9. This indicates that the micro-cantilever failure occurred at the reaction layer/SiC interface. This fracture mode was quite reproducible in several tests. This fact suggests that the micro-cantilever beam can be regarded as a homogeneous material. That assumption simplifies the calculation of bending strength in this condition, because of the similar modulus values of the W and reaction layers. Hence, the bending strength (σ) of the micro-cantilevers is derived from linear-elastic bending theory for homogeneous material [30] as:

$$\sigma = PLy/I \quad (1)$$

The elastic modulus (E) of a cantilever is based on the equation:

$$E = PL^3/3I\delta \quad (2)$$

Moreover, the fracture strain (ε) is calculated by Hooke's law:

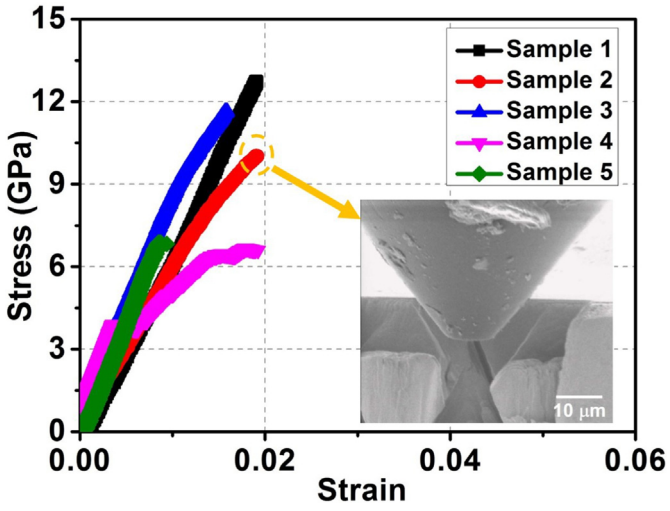

Fig. 10. The stress-strain curves of micro-cantilever bending, the inserted image is the in-situ SEM observation at maximum loading.

$$\varepsilon = \sigma/E \quad (3)$$

where P is applied bending force, L is the distance between fracture location and loading point, I is the moment of inertia of the micro-cantilever cross section, and y is the vertical distance between the upper surface and the neutral plane, δ is the vertical deflection at the loading point. For the triangle cross-section, I is $b*h^3/36$, and y is 3/h, where b and h are defined in Fig. 8. Hence, the final equations to obtain bending strength and fracture strain are:

$$\sigma = 12PL/(bh^2) \quad (4)$$

$$\varepsilon = h\delta/L^2 \quad (5)$$

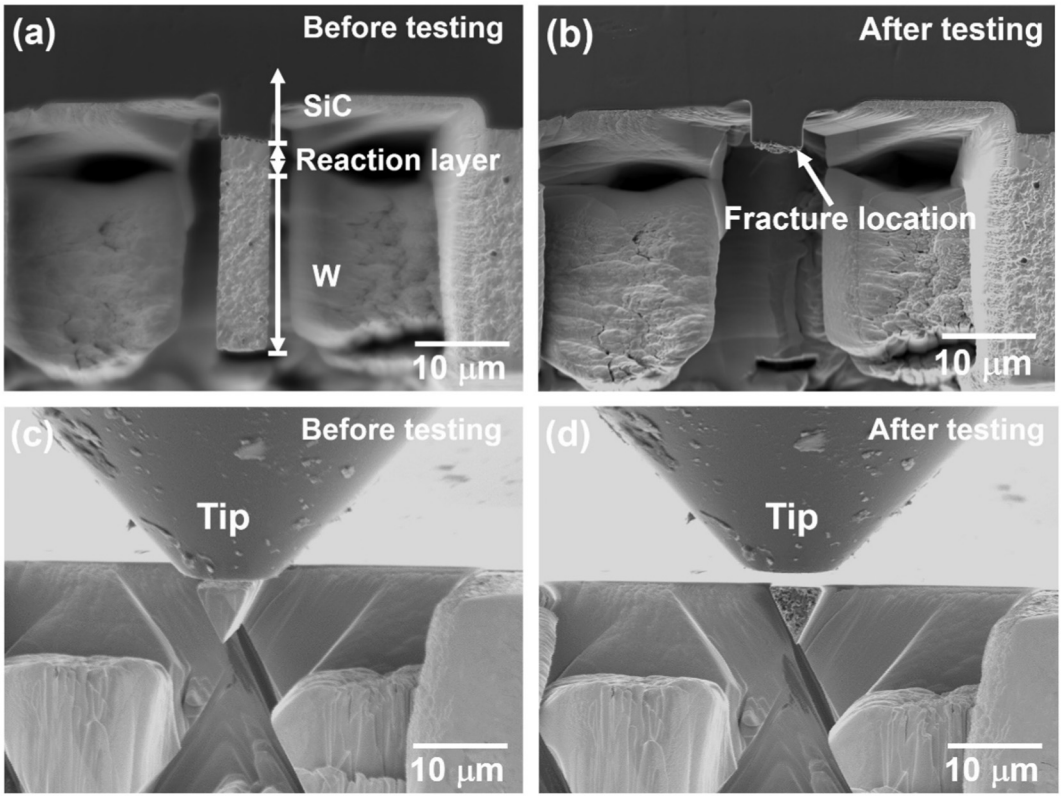

Fig. 9. SEM images of micro-cantilever before and after testing, (a) before testing from above, (b) after testing from below, (c) before testing from front, (d) after testing from front.

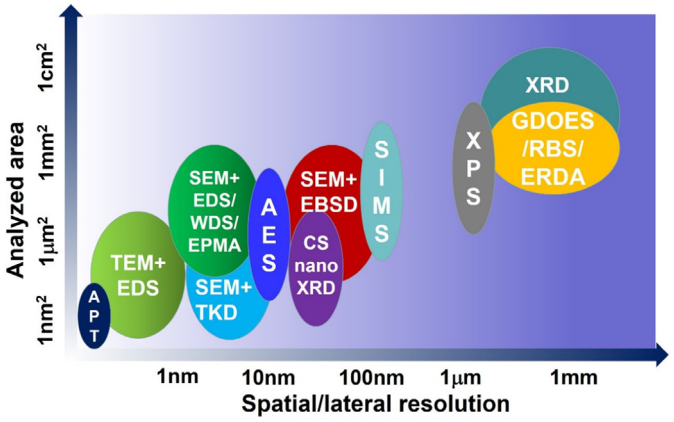

Fig. 11. The relationship between area analyzed and spatial/lateral resolution for various characterization methods.
Note:
XRD, GDOES, RBS, ERDA, XPS, SIMS, CSnanoXRD and AES offer lateral resolution.
SEM + EBSD, SEM + EDS/WDS, SEM + TKD, TEM + EDS and APT provide spatial resolution.
XRD: X-ray diffraction
GDOES: Glow-discharge optical emission spectroscopy
RBS: Rutherford backscattering spectroscopy
ERDA: Elastic recoil detection analysis
XPS: X-ray photoelectron spectroscopy
SIMS: Secondary ion mass spectrometry
CSnanoXRD: Cross-sectional X-ray nanodiffraction
AES: Auger electron spectroscopy
SEM: Scanning electron microscopy
EBSD: Electron backscatter diffraction
EDS: Energy dispersive X-ray spectroscopy
WDS: Wavelength dispersive X-ray spectroscopy
TKD: Transmission Kikuchi diffraction
TEM: Transmission electron microscopy
APT: Atom probe tomography.

Fig. 10 shows the stress-strain curves and in-situ SEM observation at maximum loading. The micro-cantilever totally failed at maximum loading, showing that the micro-cantilever bending load resulted in a brittle mode fracture without any indication of plastic deformation. The average adhesion strength reached 9.52 ± 2.68 GPa, which reveals that the W/SiC interface formed a robust interfacial bond.

4. Discussion

4.1. Phase identification for coatings on ceramics

This multiscale experimental scheme for analyzing coatings on ceramics covers a large range of analyzed area and spatial/lateral resolution, illustrated in Fig. 11. This scheme includes various microstructural characterization techniques. No single, specific characterization method can obtain such large analyzed area and high spatial/lateral resolution at the same time. An effective combination of multiscale microstructural characterization methods is necessary for phase identification. We propose an effective combination of GDOES/TEM + EDS/SEM + TKD for phase identification on coatings on ceramics system. This scheme is especially applicable to the coatings with light elements, nanocrystalline structures, and microscale thickness. It is well known that phase identification usually requires the integration of elemental distribution and crystal structure analysis methods. Thus, the feasibility of proposed combination of characterization methods is elaborated according to elemental distribution and crystal structure analysis.

For elemental distribution analysis, GDOES, AES, XPS, SIMS, RBS and ERDA are available choices for depth-resolved measurement of elements, but only GDOES and SIMS are suitable for this case ascribing to the relatively thick coating thickness (~25 μm). GDOES was proposed for elemental depth profiling because it provided a superior sputtering rate (~1 μm/min) than SIMS (sputtering speed ~10 μm/h), which enabled concentration depth profile obtained in a few minutes [8]. GDOES is capable of performing on relatively large measurement area and providing accurate elemental analysis for most elements, especially for light elements. These excellent capabilities are expected to offer average diffusion depth of elements and offset the drawbacks of EDS/WDS analysis in light elements and the elements with energy peaks overlap. Therefore the elemental depth profiling measured by GDOES is necessary for this work. As shown in Fig. 3, GDOES provided data on a macro-scale area of coating surface (approximately 12.6 mm^2), and clearly identified the light element (C) and elements with energy peaks overlap (W, M = 1.774 keV and Si, K_α = 1.739 keV) in EDS analysis. In addition, the diffusion depth of C on the coated surface was accurately detected, which implies GDOES could be used for the evaluation of impurities on coated surfaces. EDS and WDS are common methods for microscale elemental distribution analysis on coatings. EDS is frequently equipped on SEM or TEM to provide microstructural observation and elemental distribution analysis at the same time. Also, WDS is commonly equipped on SEM or electron probe microanalysis (EPMA) in practical applications. Since EDS can provide higher efficiency in elemental analysis than WDS, to compensate for the absence of microstructural observation in GDOES analysis, we chose EDS for elemental analysis. It must be pointed out that the elemental distribution analysis of EDS is not always strictly precise, due to numerous energy peaks overlaps and inaccurate light elements analysis. This technological hurdle can be overcome by integrating GDOES analysis. Since TEM + EDS is performed on a relatively small, thin TEM sample, it is expected to provide more precise elemental distribution analysis than SEM + EDS. For example, as can be seen from Fig. 5, regardless of the existence of the light element (C) and elements with energy peak overlaps (W and Si) in EDS analysis, STEM + EDS (acquired by STEM mode in TEM) was still capable of providing relatively precise elemental distribution in the reaction layer. APT is capable of offering precise elemental analysis at atomic scale. This technique will be a powerful tool in case the phase distribution is super fine so that APT sample smaller than TEM foil contains several grains.

XRD is widely used for crystal structure analysis of coatings to obtain averaged crystal structure information over numerous grains, but may be limited to the qualitative analysis on the coated surface, and is not suitable for the analysis on the cross-section of coatings in case of the thin thickness of coatings. Due to the required thickness of the W coating, planar XRD could not be used for the analysis of the diffusion layer. CSnanoXRD offers better lateral resolution than XRD and has been successfully applied to the cross-sectional analysis of coatings, as reported by Gruber et al. [31] and Zalesak et al. [32]. However, CSnanoXRD is may be available at only a synchrotron facility. To study the crystal structure of coatings on cross-sections, EBSD and TKD are good choices because they are capable of providing detailed crystal structure information for each grain. EBSD and TKD are often written as SEM + EBSD and SEM + TKD, because they are frequently equipped on SEMs in practical applications. It should be pointed out that SEM + TKD is superior to SEM + EBSD in nano-crystal structure analysis, because SEM + TKD at (2–5 nm) provides a better spatial resolution than SEM + EBSD at (25–100 nm). This is expected to be a benefit in crystal structure analysis of nanocrystalline structures. In addition, SEM + TKD and TEM can use the same specimen, doing both analyses at the same location. Therefore, SEM + TKD analysis is recommended to be combined with TEM analysis. As an example, as shown in Fig. 6, the W_2C grains with the grains size in the range of 200 nm to 1.8 μm were distinctly identified and the detailed crystal structure could be seen from Table 1, showing the powerful performance of SEM + TKD on crystal structure analysis. In some cases, SEM + TKD is incapable of successfully identifying the crystal

structures of all the grains because of crystal disordering, light elements, nano-size grains, and insensitivity; an example is the unidentified silicide in the reaction layer (Fig. 6c). In this case, traditional TEM diffraction analysis is a great complementary method to identify phases that could not identified by SEM + TKD analysis, as shown in (Fig. 5).

4.2. Adhesion strength determination for coatings on ceramics

To evaluate the adhesion strength of coatings on ceramics, micro-cantilever bending using nano-indentation system is the recommended approach. The three crucial elements of this are fabrication and testing of micro-cantilever, modulus determination, and theory or modeling. FIB milling is frequently used for the fabrication of mirco-cantilever beams, in which the principal for FIB milling is using diminishing current to protect the micro-cantilever from damage by the Ga + implantation. There is no a specific requirement for the cross-sectional shapes of the micro-cantilever beam, and various shapes such as triangles [22], rectangles [20] and polygons [21] have been reported in prior studies. The selection of theory or modeling for adhesion strength calculation is dependent on the modulus determination of the micro-cantilever. For instance, if the micro-cantilever is assumed to be a homogeneous or near homogeneous material, the adhesion strength calculation can be based on linear-elastic bending theory for homogeneous material [30] (Fig. 6 and Fig. 7). On the contrary, if the micro-cantilever is an inhomogeneous material, a new theory or modeling needs to be developed for adhesion strength determination, in which the modulus parameters are indispensable for theory or modeling. To simulate the micro-cantilever bending process, finite element modeling is one of the most promising approaches, as reported in previous studies [20]. Note that a modification of the cantilever test can provide the fracture toughness of the coating system: micro-cantilever bending of specimens with notches at the coating interface. The details can be found elsewhere [21].

For modulus determination, the high-speed nano-indentation technique is used to measure the modulus of coatings in cross-section, because conventional Vickers and Knoop gauges are not able to measure the modulus of thin coating in cross-section due to the overlarge indenter load. The applications of nano-indentation technique on the cross-section of coatings also can been seen from elsewhere [31,32]. As seen from Fig. 7, even though the coating was a relatively thin ~25 μm, the modulus in cross-section was accurately measured by the high-speed nano-indentation technique. More importantly, the high-speed nano-indentation technique can rapidly obtain modulus data from large areas, evidenced by the 16 × 40 array of indentations completed around 10 min in a 40 μm × 100 μm area.

It is noted here that the size dependence of the adhesion strength was not investigated in the micro-cantilever compression testing, and this has been a common topic in small scale mechanical property testing studies [33]. As reported by Son et al., macroscopic flexural strength of ~1GPa was obtained from W-SiC joint [34]. The value is significantly lower than the adhesion strength obtained in our work (9.52 ± 2.68 GPa), which could be explained by the size effect of specimen from macroscale to microscale. Yang et al., reported that the bending strength of a Ti_2AlC ceramic micro-cantilever beam with similar size to our work could reach up to 9.6 ± 0.4 GPa [35], contrasted to conventional macroscopic flexural strength of 432 ± 12 MPa [36]. Therefore the high bending strength obtained in our work should be reasonable for a coated SiC ceramic micro-cantilever beam. One explanation of the specimen size effect is size of defect. Since micro-cantilever is small, there is less chance to include processing defect within the cantilever, which makes material apparently strong. In case of macroscopic testing, there is more chance to have material with defect which can be fracture initiation site [37]. In addition, the fabricated micro-cantilever beam that we used has a long W arm, and the fracture surface was found at the interface of the reaction layer and the SiC substrate. The superiority of micro-cantilever bending for evaluating the adhesion strength can be seen from Fig. 9 and Fig. 10, where the system provided in-situ observation and adhesion strength measurement with failure at the joint interface. This fact demonstrates that the micro-cantilever bending is useful for adhesion strength evaluation of coatings on ceramics systems.

The microstructural characterization conducted in this study provides a better understanding of the micro-cantilever bending strength. Based on the appearance of the fracture in Fig. 9b, the specimens failed at the interface between the SiC substrate and the reaction layer consisting of the W_2C and W_5Si_3 phases. It is known that a CTE mismatch among different phases significantly affects the bonding strength [38]. The formation of W_2C and W_5Si_3 inevitably enhances the CTE mismatch at the interface because they have relatively high CTEs (W_2C, CTE: $5.1 \times 10^{-6} K^{-1}$ [39]; W_5Si_3, a: $5.0 \times 10^{-6} K^{-1}$, c: $16.3 \times 10^{-6} K^{-1}$ [40]) compared with W (CTE: $4.5 \times 10^{-6} K^{-1}$) and SiC (CTE: $4.0 \times 10^{-6} K^{-1}$). Since the CTE of W_5Si_3 along the c axis is significant, it is possible that the SiC/W_5Si_3 interface was relatively weak. The TEM diffraction analysis suggested no grain texture in W_5Si_3, and STEM-EDS analysis showed that the W_5Si_3 and W_2C phases were randomly distributed within the reaction layer. Therefore, a relatively weak interface also was present randomly and caused deviations in the cantilever bending strength.

5. Conclusions

A coating/ceramic substrate system (W/SiC) was investigated using several techniques to demonstrate a multiscale experimental characterization scheme useful to assessing coatings on ceramic substrates. The proposed evaluation methods for phase identification and adhesion strength evaluation are as follows:

1. A combination of GDOES, TEM + EDS, SEM + TKD characterization is used for phase identification, in which SEM + TKD provides superior spatial resolution for phase identification.
2. Micro-cantilever bending using a nano-indentation system is used for adhesion strength evaluation, in which fabrication of micro-cantilever, modulus determination by the high-speed nano-indentation technique and corresponding theory or modeling are essential for accurate adhesion strength determination. The high-speed nano-indentation technique is especially valuable in allowing modulus determination on large measurement areas in a relatively short time.

Acknowledgements

The study was supported by the US DOE Office of Fusion Energy Sciences under contract DE-AC05-00OR22725 with UT-Battelle, LLC. The first author was supported by the program of China Scholarship Council [grant number 201706690006]. Austin Schumacher and Michael Trammell at Oak Ridge National Laboratory (ORNL) contributed SPS experiments. The authors wish to thank Frederick Wiffen and Peter A. Mouche at ORNL for valuable comments on this manuscript.

References

[1] C.B. Carter, M.G. Norton, Ceramic Materials: Science and Engineering, Springer Science & Business Media, Berlin, 2007.
[2] K. Herrmann, R. Leneis, A. Thimm, A. Dohn, Metal coating on ceramic substrates, U. S. Patent Application 14/895, 782; 2016.
[3] W.A. Mohrez, A. Kohyama, H. Kishimoto, Y. Kohno, Effect of 10 MW/m^2 plasma exposure on W-SiC/SiC dual layer tiles, Fusion Eng. Des. 88 (9–10) (2013) 1655–1659.
[4] Z. Chen, K. Zhou, X. Lu, Y.C. Lam, A review on the mechanical methods for evaluating coating adhesion, Acta Mech. 225 (2) (2014) 431–452.
[5] M. Tkadletz, N. Schalk, R. Daniel, J. Keckes, C. Czettl, C. Mitterer, Advanced characterization methods for wear resistant hard coatings: a review on recent

progress, Surf. Coat. Tech. 285 (2016) 31–46.
[6] P.Y. Jouan, M.C. Peignon, C. Cardinaud, G. Lemperiere, Characterisation of TiN coatings and of the TiN/Si interface by X-ray photoelectron spectroscopy and Auger electron spectroscopy, Appl. Surf. Sci. 68 (4) (1993) 595–603.
[7] K. Rokosz, T. Hryniewicz, S. Raaen, P. Chapon, Ł. Dudek, GDOES, XPS, and SEM with EDS analysis of porous coatings obtained on titanium after plasma electrolytic oxidation, Surf. Interface Anal. 49 (4) (2017) 303–315.
[8] R.E. Galindo, R. Gago, D. Duday, C. Palacio, Towards nanometric resolution in multilayer depth profiling: a comparative study of RBS, SIMS, XPS and GDOES, Anal. Bioanal. Chem. 396 (8) (2010) 2725–2740.
[9] R. Rachbauer, E. Stergar, S. Massl, M. Moser, P.H. Mayrhofer, Three-dimensional atom probe investigations of Ti-Al-N thin films, Scr. Mater. 61 (2009) 725–728.
[10] D. Stojakovic, Electron backscatter diffraction in materials characterization, Process. Appl. Ceram. 6 (2012) 1–13.
[11] J. Keckes, R. Daniel, J. Todt, J. Zalesak, B. Sartory, S. Braun, J. Gluch, M. Rosenthal, M. Burghammer, C. Mitterer, S. Niese, A. Kubec, 30 nm X-ray focusing correlates oscillatory stress, texture and structural defect gradients across multilayered TiN-SiO_x thin film, Acta Mater. 144 (2018) 862–873.
[12] B. Li, X. Fan, K. Zhou, T. Wang, A semi-analytical model for predicting stress evolution in multilayer coating systems during thermal cycling, Inj. J. Mech. Sci. 135 (2018) 31–42.
[13] B. Li, X. Fan, T. Wang, K. Zhou, Interfacial fracture behavior of double-ceramic-layer thermal barrier coating system with segmented structure, Eng. Fract. Mech. 201 (2018) 13–28.
[14] S.J. Bull, Nanoindentation of coatings, J. Phys. D. Appl. Phys. 38 (2005) R393–R413.
[15] B. Wang, T. Siegmund, A modified 4-point bend delamination test, Microelectron. Eng. 85 (2) (2008) 477–485.
[16] J. Tong, K.Y. Wong, C. Lupton, Determination of interfacial fracture toughness of bone–cement interface using sandwich Brazilian disks, Eng. Fract. Mech. 74 (12) (2007) 1904–1916.
[17] S.J. Bull, E.G. Berasetegui, An overview of the potential of quantitative coating adhesion measurement by scratch testing, Tribol. Int. 39 (2) (2006) 99–114.
[18] M. Nase, A. Zankel, B. Langer, H.J. Baumann, W. Grellmann, P. Poelt, Investigation of the peel behavior of polyethylene/polybutene-1 peel films using in situ peel tests with environmental scanning electron microscopy, Polymer 49 (25) (2008) 5458–5466.
[19] D.E.J. Armstrong, A.J. Wilkinson, S.G. Roberts, Measuring anisotropy in Young's modulus of copper using microcantilever testing, J. Mater. Res. 24 (11) (2009) 3268–3276.
[20] F. Iqbal, J. Ast, M. Göken, K. Durst, In situ micro-cantilever tests to study fracture properties of NiAl single crystals, Acta Mater. 60 (3) (2012) 1193–1200.
[21] D.D. Maio, S.G. Roberts, Measuring fracture toughness of coatings using focused-ion-beam-machined microbeams, J. Mater. Res. 20 (2) (2005) 299–302.
[22] D.E.J. Armstrong, C.D. Hardie, J.S.K.L. Gibson, A.J. Bushby, P.D. Edmondson, S.G. Roberts, Small-scale characterisation of irradiated nuclear materials: part II nanoindentation and micro-cantilever testing of ion irradiated nuclear materials, J. Nucl. Mater. 462 (2015) 374–381.
[23] K. Matoy, T. Detzel, M. Müller, C. Motz, G. Dehm, Interface fracture properties of thin films studied by using the micro-cantilever deflection technique, Surf. Coat. Tech. 204 (6–7) (2009) 878–881.
[24] L.L. Snead, T. Nozawa, Y. Katoh, T.S. Byun, S. Kondo, D.A. Petti, Handbook of SiC properties for fuel performance modeling, J. Nucl. Mater. 371 (1–3) (2007) 329–377.
[25] K. Wang, R.R. Reeber, The role of defects on thermophysical properties: thermal expansion of V, Nb, ta, Mo and W, Mater. Sci. Eng. R. Rep. 23 (1998) 101–137.
[26] Product Sheet from Dow Chemical Company, https://www.dow.com/assets/attachments/business/gt/advanced_ceramics/cvd_silicon_carbide/tds/cvd_silicon_carbide.pdf.
[27] Z. Zhang, E. Hasenhuetl, K. Yabuuchi, A. Kimura, Evaluation of helium effect on ion-irradiation hardening in pure tungsten by nano-indentation method, Nucl. Mater. Energy 9 (2016) 539–546.
[28] G.P. Škoro, J.R.J. Bennett, T.R. Edgecock, S.A. Gray, A.J. McFarland, C.N. Booth, K.J. Rodgers, J.J. Back, Dynamic Young's moduli of tungsten and tantalum at high temperature and stress, J. Nucl. Mater. 409 (1) (2011) 40–46.
[29] T. Chen, L. Tan, Z. Lu, H. Xu, The effect of grain orientation on nanoindentation behavior of model austenitic alloy Fe-20Cr-25Ni, Acta Mater. 138 (2017) 83–91.
[30] L.L. Bucciarelli, Engineering Mechanics for Structures, Dover Publications, New York, 2008.
[31] D.P. Gruber, J. Todt, N. Wöhrl, J. Zalesak, M. Tkadletz, A. Kubec, S. Niese, M. Burghammer, M. Rosenthal, H. Sternschulte, M.J. Pfeifenberger, B. Sartory, J. Keckes, Gradients of microstructure, stresses and mechanical properties in a multi-layered diamond thin film revealed by correlative cross-sectional nano-analytics, Carbon 144 (2019) 666–674.
[32] J. Zalesak, M. Bartosik, R. Daniel, C. Mitterer, C. Krywka, D. Kiener, P.H. Mayrhofer, J. Keckes, Cross-sectional structure-property relationship in a graded nanocrystalline $Ti_{1-x}Al_xN$ thin film, Acta Mater. 102 (2016) 212–219.
[33] S.H. Chen, B. Feng, Size effect in micro-scale cantilever beam bending, Acta Mech. 219 (3–4) (2011) 291–307.
[34] S.J. Son, K.H. Park, Y. Katoh, A. Kohyama, Interfacial reactions and mechanical properties of W–SiC in-situ joints for plasma facing components, J. Nucl. Mater. 329 (2004) 1549–1552.
[35] H.J. Yang, Y.T. Pei, G.M. Song, J.T.M.D. Hosson, Healing performance of Ti_2AlC ceramic studied with in situ microcantilever bending, J. Eur. Ceram. Soc. 33 (2) (2013) 383–391.
[36] Y. Bai, X. He, C. Zhu, G. Chen, Microstructures, electrical, thermal, and mechanical properties of bulk Ti_2AlC synthesized by self-propagating high-temperature combustion synthesis with Pseudo hot isostatic pressing, J. Am. Ceram. Soc. 95 (1) (2012) 358–364.
[37] Z.P. Bažant, Size effect on structural strength: a review, Arch. Appl. Mech. 69 (9–10) (1999) 703–725.
[38] H.P. Kirchner, J.C. Conway Jr., A.E. Segall, Effect of joint thickness and residual stresses on the properties of ceramic adhesive joints: I, finite element analysis of stresses in joints, J. Am. Ceram. Soc. 70 (2) (1987) 104–109.
[39] P.A. Dearnley, Introduction to Surface Engineering, Cambridge University Press, Cambridge, 2017.
[40] G. Rodrigues, V.M. Chad, C.A. Nunes, P.A. Suzuki, G.C. Coelho, Thermal expansion of the W_5Si_3 and T_2 phases of the W–Si–B system investigated by high-temperature X-ray diffraction, Intermetallics 15 (3) (2007) 241–244.